

# Inducing High Ionic Conductivity in the Lithium Superionic Argyrodites $\text{Li}_{6+x}\text{P}_{1-x}\text{Ge}_x\text{S}_5\text{I}$ for All-Solid-State Batteries

Marvin A. Kraft,<sup>†</sup> Saneyuki Ohno,<sup>†,‡,ID</sup> Tatiana Zinkevich,<sup>§,||</sup> Raimund Koerver,<sup>†,‡</sup> Sean P. Culver,<sup>†,‡</sup> Till Fuchs,<sup>†,‡</sup> Anatoliy Senyshyn,<sup>⊥</sup> Sylvio Indris,<sup>§,||,ID</sup> Benjamin J. Morgan,<sup>#</sup> and Wolfgang G. Zeier<sup>\*†,‡,§,ID</sup>

<sup>†</sup>Institute of Physical Chemistry, Justus-Liebig-University Giessen, Heinrich-Buff-Ring 17, D-35392 Giessen, Germany

<sup>‡</sup>Center for Materials Research (LaMa), Justus-Liebig-University Giessen, Heinrich-Buff-Ring 16, D-35392 Giessen, Germany

<sup>§</sup>Institute for Applied Materials, Karlsruhe Institute of Technology, Hermann-von-Helmholtz Platz 1, D-76344 Eggenstein-Leopoldshafen, Germany

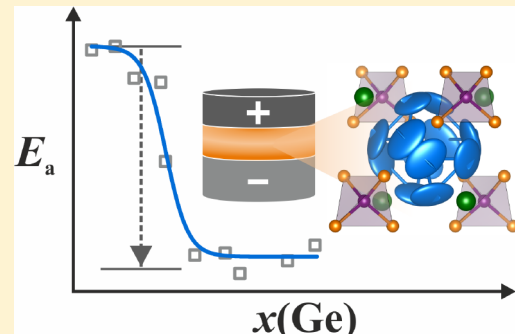
<sup>||</sup>Helmholtz Institute Ulm, Helmholtzstraße 11, 89081 Ulm, Germany

<sup>⊥</sup>Heinz Maier-Leibnitz Zentrum, Technische Universität München, 85748 Garching, Germany

<sup>#</sup>Department of Chemistry, University of Bath, Claverton Down, Bath BA2 7AY, U.K.

## S Supporting Information

**ABSTRACT:** Solid-state batteries with inorganic solid electrolytes are currently being discussed as a more reliable and safer future alternative to the current lithium-ion battery technology. To compete with state-of-the-art lithium-ion batteries, solid electrolytes with higher ionic conductivities are needed, especially if thick electrode configurations are to be used. In the search for optimized ionic conductors, the lithium argyrodites have attracted a lot of interest. Here, we systematically explore the influence of aliovalent substitution in  $\text{Li}_{6+x}\text{P}_{1-x}\text{Ge}_x\text{S}_5\text{I}$  using a combination of X-ray and neutron diffraction, as well as impedance spectroscopy and nuclear magnetic resonance. With increasing Ge content, an anion site disorder is induced and the activation barrier for ionic motion drops significantly, leading to the fastest lithium argyrodite so far with  $5.4 \pm 0.8 \text{ mS cm}^{-1}$  in a cold-pressed state and  $18.4 \pm 2.7 \text{ mS cm}^{-1}$  upon sintering. These high ionic conductivities allow for successful implementation within a thick-electrode solid-state battery that shows negligible capacity fade over 150 cycles. The observed changes in the activation barrier and changing site disorder provide an additional approach toward designing better performing solid electrolytes.



## 1. INTRODUCTION

Solid-state batteries provide a possibility for energy storage with higher energy densities and improved safety by using a solid electrolyte and lithium metal anode, as compared to using liquid electrolytes.<sup>1–7</sup> There have been many recent advances in the field concerning a better understanding of the interfacial reactions,<sup>8–10</sup> the employment of coatings,<sup>11,12</sup> the minimized use of carbon additives,<sup>13–15</sup> strain design and particle size optimization in the electrodes.<sup>16–18</sup> However, the challenge for thick electrode configurations<sup>19</sup> still remains: the use of solid electrolytes in thick electrode configurations is currently limited by the low ionic conductivity of solid electrolytes.<sup>2,19</sup> Electrolytes with high ionic conductivities are needed to achieve higher energy densities.

Recently, among all of the well-performing lithium thiophosphates, such as the  $\text{Li}_2\text{S}-\text{P}_2\text{S}_5$  glass phases and  $\text{Li}_{10}\text{MP}_2\text{S}_{12}$  ( $\text{M} = \text{Ge}, \text{Sn}$ )<sup>20–29</sup> the class of argyrodites  $\text{Li}_6\text{PS}_3\text{X}$  ( $\text{X} = \text{Cl}, \text{Br}, \text{I}$ ) has attracted considerable interest.<sup>30–34</sup> The crystal structure of  $\text{Li}_6\text{PS}_3\text{X}$  is shown in Figure 1. In a fully ordered arrangement, the halide anions  $\text{X}^-$  form a face-centered cubic lattice (Wyckoff 4a) with  $\text{PS}_4^{3-}$  tetrahedra on the

octahedral sites (P on Wyckoff 4b) and the free  $\text{S}^{2-}$  in half of the tetrahedral sites (Wyckoff 4d). Diffusion in solid electrolytes is usually analyzed in terms of jumps between individual sites.<sup>35</sup> Crystallographic studies in the argyrodites have identified two distinct  $\text{Li}^+$  positions, namely, the 48h and 24g Wyckoff positions, which form  $\text{Li}^+$  cages around the free  $\text{S}^{2-}$  on Wyckoff 4d. Within a site-jump model of lithium diffusion there are three inequivalent jumps: 48h–24g–48h (doublet jump), 48h–48h within the cage (intracage jump), and 48h–48h between the cages (intercage jump).<sup>30,33</sup> For  $\text{X} = \text{Cl}$  and  $\text{Br}$  the  $\text{S}^{2-}$  and  $\text{X}^-$  positions exhibit a significant fraction of anion site disorder.<sup>32–34,36</sup> If iodine is the halide in the structure, no site disorder occurs due to the large size mismatch between  $\text{S}^{2-}$  and  $\text{I}^-$ ,<sup>30</sup> opening up the question as to whether the site disorder can be influenced further. Kraft et al. have recently shown that the absence of the disorder in the iodine-containing argyrodites is associated with high activation barriers for ion migration and a low ionic conductivity of  $1.3 \times 10^{-6} \text{ S cm}^{-1}$ .<sup>30</sup> While

Received: September 23, 2018

Published: November 1, 2018

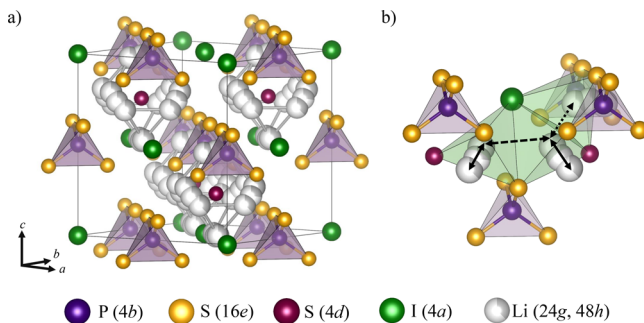


**Figure 1.** (a) Crystal structure of  $\text{Li}_6\text{PS}_5\text{X}$  ( $\text{X} = \text{I}$ ), in which the  $\text{I}^-$  form a face-centered cubic lattice, with  $\text{PS}_4$  tetrahedra in the octahedral voids and a free  $\text{S}^{2-}$  on half of the tetrahedral vacant sites ( $4d$ ). The  $\text{Li}^+$  forms pseudo-octahedral cages around the  $\text{S}^{2-}$  site with two crystallographically distinct positions,  $24g$  and  $48h$ . (b) For lithium transport effected by discrete jumps between sites, the rate-determining step is the intercage  $48h$ - $48h$  jump, as shown by the  $\text{LiS}_3\text{I}$  polyhedra. This requires lithium to move past a window of the  $4a$  iodine site and the sulfur of the  $\text{PS}_4$  tetrahedra.

substitutions have been performed mostly on the anion sites in the argyrodites, a recent study shows the possibility of aliovalent doping in  $\text{Li}_{6+x}\text{P}_{1-x}\text{Si}_x\text{S}_5\text{Br}$ ,<sup>31</sup> producing an increase in the ionic conductivity. It should be noted however that the incorporation of  $\text{Ge}^{4+}$  in  $\text{Li}_6\text{PS}_5\text{Br}$  was not possible due to the larger ionic radius of  $\text{Ge}^{4+}$  in the smaller lattice volume in  $\text{Li}_6\text{PS}_5\text{Br}$ .

Inspired by the possibility of incorporating Ge into a composition possessing a larger unit cell, we have investigated the effect of  $\text{Ge}^{4+}$  substitution in  $\text{Li}_{6+x}\text{P}_{1-x}\text{Ge}_x\text{S}_5\text{I}$  on the structure-transport relationships. Using a combination of Rietveld refinements against neutron and X-ray diffraction data, we identify the underlying structural changes associated with the Li and anion substructures including changes to the site disorder. Impedance spectroscopy and lithium nuclear magnetic resonance were used to monitor the changing ionic transport. With increasing Ge fraction, the diffusion pathways for  $\text{Li}^+$  expand and site disorder between the  $\text{S}^{2-}$  and  $\text{I}^-$  positions appears. The increasing disorder is correlated to a sharp decrease in the activation barrier and an increase in the conductivity over orders of magnitude, leading to the highest in lithium reported so far with  $\sigma = 5.4 \pm 0.8 \text{ mS cm}^{-1}$ , when cold-pressed, and  $\sigma = 18.4 \pm 2.7 \text{ mS cm}^{-1}$  upon sintering. We further show that this fast ionic conductor can be used to build solid-state batteries with thick anode and cathode layers, exhibiting stable capacities for at least 150 cycles, even at higher C-rates. This work demonstrates that inducing disorder in materials using elemental substitutions is a promising approach to alter the potential energy landscape tailoring the ionic conductivity of solid electrolytes for better performing all-solid-state batteries.

## 2. EXPERIMENTAL METHODS

**Synthesis.** All preparations and sample treatments for  $\text{Li}_{6+x}\text{P}_{1-x}\text{Ge}_x\text{S}_5\text{I}$  were carried out under an argon atmosphere. Lithium sulfide ( $\text{Li}_2\text{S}$ , Sigma-Aldrich, 99.98%), phosphorus pentasulfide ( $\text{P}_2\text{S}_5$ , Sigma-Aldrich, 99%), germanium sulfide ( $\text{GeS}$ , Alpha Aesar, 99.99%), sulfur (S, Acros Organics, 99.999%), and  $\text{LiI}$  (Alpha Aesar, 99.995%) were mixed in the appropriate stoichiometric ratio. Before the synthesis, all precursors were thoroughly dried and sulfur was sublimated. All mixtures were hand ground in an agate mortar, pressed into pellets, and then filled into quartz ampoules (10 mm inner diameter and 10–12 cm in length), which were sealed under vacuum. All ampoules were carbon-coated and preheated at 800 °C under dynamic vacuum to avoid all traces of water in the reaction atmosphere. The reactions were

performed at 550 °C for 2 weeks in order to ensure a complete reaction. The obtained mixture was subsequently ground and isostatically pressed into pellets (10 mm diameter) for the impedance measurements or kept as powder for the diffraction studies.

**Neutron Powder Diffraction.** High-resolution neutron powder diffraction data collection on the argyrodite samples  $\text{Li}_{6+x}\text{P}_{1-x}\text{Ge}_x\text{S}_5\text{I}$  with  $x = 0, 0.15, 0.25, 0.3$ , and  $0.6$  was performed in a Debye–Scherrer geometry at the Heinz Maier-Leibnitz Zentrum (research reactor FRM II, Garching b. München, Germany) on the high-resolution diffractometer SPODI.<sup>37</sup> Data collection was performed using one wavelength, i.e., monochromatic neutrons ( $\lambda = 1.548\ 17(2)$  Å) that were obtained from the thermal neutron beam at a 155° takeoff angle using the 551 and 331 reflections of a vertically focused composite Ge monochromator of 200 mm height. The vertical-position-sensitive multidetector (300 mm vertical sensitivity range at 1.117 m sample-to-detector distance) consisting of 80  $^3\text{He}$  tubes and covering an angular range of 160°  $2\theta$  was used for data collection. The samples (approximately 2 cm<sup>3</sup> in volume) were filled into a thin-wall (0.15 mm) vanadium can of 12 mm in diameter under an argon atmosphere and then metal-sealed using indium wire. The vanadium container was then mounted on a capillary spinner enabling sample rotation and, thus, minimizing effects of preferred crystallite orientations. Two-dimensional powder diffraction data of the continuously rotated sample were collected and corrected for geometrical aberrations and detector nonlinearities.<sup>38</sup>

**X-ray Powder Diffraction.** X-ray diffraction measurements of  $\text{Li}_{6+x}\text{P}_{1-x}\text{Ge}_x\text{S}_5\text{I}$  were carried out on a PANalytical Empyrean powder diffractometer in Bragg–Brentano  $\theta$ - $\theta$  geometry with  $\text{Cu K}\alpha$  radiation. Measurements were carried out in the  $2\theta$  range between 10° and 90° with a step size of 0.026°. The counting time per step was 300 s. All powders were placed on (911)-oriented silicon zero background holders and sealed using a 7.5 μm thick Kapton polyimide film.

**Rietveld Analysis.** Rietveld refinements were carried out using the TOPAS-Academic V6 software package.<sup>39</sup> Similar to recent work on  $\text{Li}_{10}\text{GeP}_2\text{S}_{12}$ ,<sup>25</sup> a  $2\theta$  range of 10–26.5° was excluded from the refinements of X-ray diffractions in order to mitigate the interfering diffraction intensity from the polyimide film background. The resultant structural data obtained with excluding the lower  $2\theta$  range are in good agreement with those from the neutron diffraction data over the whole measured  $2\theta$  range. The peak profile shape was described by a pseudo-Voigt function using the modified Thomson–Cox–Hastings setting.<sup>40</sup> Fit indicators  $R_{wp}$  and  $R_{exp}$  and the goodness-of-fit  $S$  were used to assess the quality of the refined structural models.<sup>41</sup> The following parameters were initially refined: (1) scale factor, (2) 30 coefficients for a Chebyshev background, (3) peak shape, (4) lattice parameters including sample displacement, (5) fractional atomic coordinates, (6) isotropic atomic displacement parameters. Finally (7), atomic occupancies of the anions were then allowed to refine simultaneously with all other parameters, to quantify the anion site disorder.

**Electrochemical Impedance Spectroscopy.** Electrical conductivities were measured by ac impedance spectroscopy, using pellets with vapor-deposited gold layers. Electrochemical impedance spectroscopy (EIS) was conducted in the temperature range of –20 to 60 °C using a VMP300 impedance analyzer (Bio-Logic Science Instruments) at frequencies from 7 MHz to 100 mHz with an amplitude of 10 mV. All fits were performed using the RelaxIS software package (rhd Instruments, version 3).

**Nuclear Magnetic Resonance.** Variable-temperature  $T_1$  and quadrupolar echo experiments have been performed on a Bruker NMR spectrometer operating at a lithium ( $^7\text{Li}$ ) frequency of 77.8 MHz. All experiments were performed in the static mode. Quadrupolar echo experiments were acquired to estimate temperature-induced line narrowing, which reports on the dynamics in kHz frequency range. The pulse sequence consisted of two 90° pulses separated by a 30 μs echo delay; after the second 30 μs echo delay acquisition started. Sixty-four scans have been collected to obtain a spectrum at each temperature, and a recycle delay of 5 s was found to be sufficient to obtain full restoration of the initial spin state before each repetition. Full-width at half-height (fwhh) has been used as a measure of motional averaging of the “rigid” line width. For  $T_1$ -relaxation time measure-

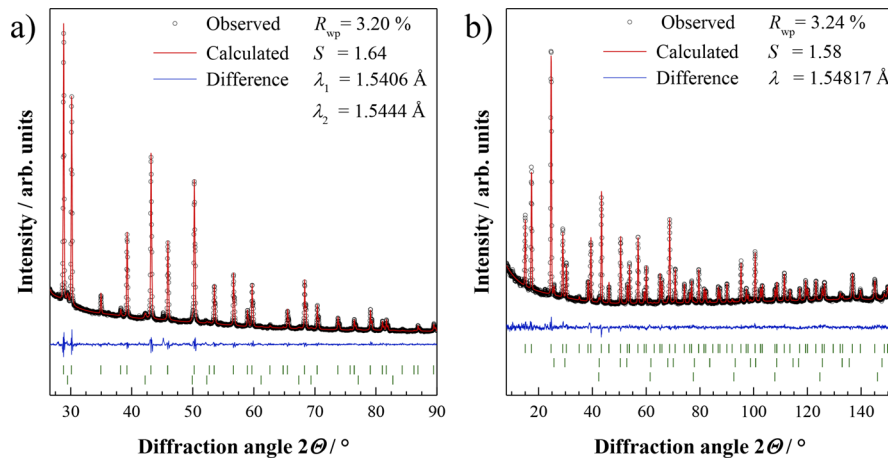


**Figure 2.** Representative X-ray (a) and neutron (b) diffraction pattern of  $\text{Li}_{6.6}\text{P}_{0.4}\text{Ge}_{0.6}\text{S}_5\text{I}$  and the corresponding Rietveld refinements. Small fractions of impurity phases can be found that correspond to  $\sim 1.6$  wt % LiI in the X-ray diffraction data and  $\sim 3.4$  wt % LiI in the neutron diffraction data, along with reflections of the V sample holder.  $R_{wp}$  and  $S$  are weighted profile R-factor and goodness of fit, respectively.

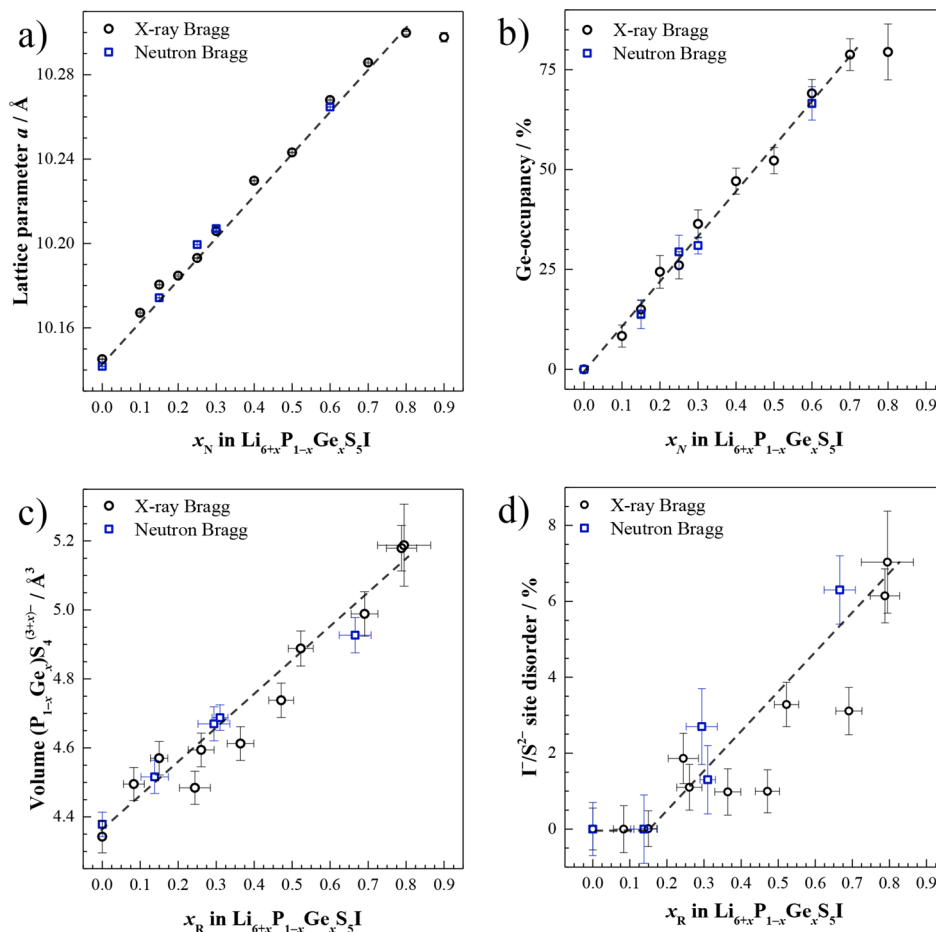


**Figure 3.** (a) Lattice parameters of the solid solutions  $\text{Li}_{6+x}\text{P}_{1-x}\text{Ge}_x\text{S}_5\text{I}$  vs nominal Ge content  $x_N$ . With increasing  $\text{Ge}^{4+}$  content, the unit cell increases until a solubility limit is reached that corresponds to the maximum solubility of  $\sim 70\%$   $\text{Ge}^{4+}$  on the  $\text{P}^{5+}$  position as shown in (b). (c) Increasing  $(\text{P}/\text{Ge})\text{S}_4$  tetrahedral volume during the substitution of the larger  $\text{Ge}^{4+}$  for  $\text{P}^{5+}$  against the refined Ge occupancy  $x_R$ . (d) While the undoped I-aryrodite is known to exhibit no site disorder,<sup>30</sup> the substitution with Ge leads to a growing  $\text{S}^{2-}/\text{I}^-$  disorder starting around 20 at. % of  $\text{Ge}^{4+}$ .

ments a saturation-recovery pulse sequence has been used. Relaxation delays have been varied from 1 ms up to 10 s, and 16 transitions have been accumulated to gain each point of the relaxation buildup curve. After acquisition, a single-exponential function has been fitted to the experimental relaxation data to get a characteristic relaxation time  $T_1$ .

**Cell Assembly.** All-solid-state battery cells using the  $\text{Li}_{6.6}\text{P}_{0.4}\text{Ge}_{0.6}\text{S}_5\text{I}$  electrolyte in combination with a  $\text{LiNi}_{0.6}\text{Co}_{0.2}\text{Mn}_{0.2}\text{O}_2$

(NCM-622) cathode and a  $\text{Li}_4\text{Ti}_5\text{O}_{12}$  (LTO) anode (both provided by BASF SE) were assembled inside of a hot-press setup under an argon atmosphere. The diameter of the cell was 12 mm. Details on the setup are provided in a previous publication.<sup>42</sup> Prior to use, the active materials were dried in a vacuum Büchi oven at 250 °C overnight. The cathode composite was prepared in an agate mortar consisting of NCM-622 and SE in a mass ratio of 70:30. A total of 55 mg of the cathode

composite was used, corresponding to an areal loading of 6.80 mAh cm<sup>-2</sup> and a thickness of approximately 160  $\mu$ m. A mass of 150 mg of solid electrolyte served as a separator (thickness  $\sim$ 450  $\mu$ m). The anode composite consisted of LTO and SE in a mass ratio of 50:50. A mass of 91 mg of the anode composite was employed (capacity = 7.04 mAh cm<sup>-2</sup>), resulting in an anode thickness of 340  $\mu$ m. The layered powders were compressed at 30 kN ( $\sim$ 2650 bar) and heated to 60 °C. The conditions were maintained during electrochemical experiments.

The battery cycling and EIS on the complete cell were carried out using an SP-150 potentiostat/galvanostat (Bio-Logic Science Instruments). The galvanostatic cycling was performed at a C-rate of 0.25 C (1.71 mA cm<sup>-2</sup>), C-rate of 0.5 C (3.42 mA cm<sup>-2</sup>), and C-rate of 1 C (6.84 mA cm<sup>-2</sup>) in a voltage range of 1.10–2.75 V vs Li<sub>4</sub>Ti<sub>5</sub>O<sub>12</sub>/Li<sub>7</sub>Ti<sub>5</sub>O<sub>12</sub>, corresponding to approximately 2.65–4.30 V vs Li<sup>+</sup>/Li. The current density was calculated based on a theoretical capacity of 200 mAh g<sup>-1</sup> of the cathode active material. After electrochemical relaxation of 30 min, EIS measurements were conducted with an amplitude of 20 mV in a frequency range of 1 MHz to 0.1 Hz.

**Scanning Electron Microscopy and Energy Dispersive X-ray Analysis.** Cross-sectional images of the battery stack after disassembly were obtained on a Merlin high-resolution scanning electron microscope (Carl Zeiss AG, Germany). The samples were transferred from a glovebox in the analysis chamber under an argon atmosphere using a transfer vessel (Leica EM VC500). EDX analysis was conducted using an XMAX EXTREME EDX detector (Oxford Instruments, United Kingdom). Measurements were carried out by application of an acceleration voltage of 5 kV and a probing current of 1000 pA.

### 3. RESULTS

**Structural Characterization.** The Li<sup>+</sup> superionic argyrodites Li<sub>6+x</sub>P<sub>1-x</sub>Ge<sub>x</sub>S<sub>5</sub>I have been synthesized with increasing Ge<sup>4+</sup>/P<sup>5+</sup> ratios in order to study the structural changes and assess the effect of the increasing lithium content on the ionic conductivity. For the structural characterization, X-ray diffraction was performed on all samples. Moreover, due to the low X-ray form factor of Li<sup>+</sup>, selected samples of  $x$  = 0, 0.15, 0.25, 0.3, and 0.6 were also investigated using neutron diffraction to better probe the changing Li<sup>+</sup> substructure. These sample compositions were selected based on the occurring changes in the ionic transport (*vide infra*).

Figure 2 shows a representative Rietveld refinement of an X-ray and a neutron diffraction pattern for the compound with the nominal composition Li<sub>6.6</sub>P<sub>0.4</sub>Ge<sub>0.6</sub>S<sub>5</sub>I. All samples exhibit minor impurity phase fractions of LiI and/or Li<sub>4</sub>GeS<sub>4</sub> in the diffraction data for the series of solid solutions (see Tables S1–S16 in Supporting Information). The minor impurities are unlikely to affect the ionic transport,<sup>30,31</sup> and the obtained structural data of all solid solutions, obtained via Rietveld refinement against laboratory X-ray and neutron diffraction patterns, can also be found tabulated in the Supporting Information. Recently, we have shown that the Si<sup>4+</sup> substitution was possible in Li<sub>6+x</sub>P<sub>1-x</sub>Si<sub>x</sub>S<sub>5</sub>Br up to 30 at. %, whereas the incorporation of Ge<sup>4+</sup> was unsuccessful.<sup>31</sup> Here in Li<sub>6+x</sub>P<sub>1-x</sub>Ge<sub>x</sub>S<sub>5</sub>I, the refined lattice parameters show an increasing unit cell volume up to 80 at. % Ge, corresponding to the formation of a solid solution (Figure 3a). However, the samples of  $x$  = 0.8, 0.9, and 1.0 exhibit high fractions of the impurity phase Li<sub>4</sub>GeS<sub>4</sub> (see Supporting Information Figure S1), indicating that a solubility limit has been reached. A Rietveld refinement of the occupancies of Ge on Wyckoff 4b shows an increasing occupancy of Ge up to 70 at. % (Figure 3b). At higher nominal Ge contents,  $x_N$ , the Ge occupancy remains constant and only the amount of the impurity phase Li<sub>4</sub>GeS<sub>4</sub> increases. The refinement of the Ge occupancy in the  $x$  = 0.9 sample is not possible due to the large amount of overlapping impurity reflections. The minor

discrepancy between the solubility limits of the lattice volume ( $x$  = 0.8) and the Ge occupancy ( $x$  = 0.7) is likely due to the larger uncertainty on the refined occupancy coming from overlapping reflections of the main phase with the Li<sub>4</sub>GeS<sub>4</sub> impurity phase. While there seems to be a degree of uncertainty on the exact solubility limit, full solid solutions of Li<sub>6+x</sub>P<sub>1-x</sub>Ge<sub>x</sub>S<sub>5</sub>I can be synthesized up to a composition of at least Li<sub>6.7</sub>P<sub>0.3</sub>Ge<sub>0.7</sub>S<sub>5</sub>I. Despite the solubility limit, the samples with  $x$  = 0.8 are included in the following structural and transport data, whenever applicable, to allow for a discussion beyond the solubility limit in this material. In addition, in order to allow for a better discussion of the data, all subsequent data are shown against the refined Ge fraction  $x_R$ , as obtained from the neutron and X-ray diffraction data, respectively.

With increasing Ge<sup>4+</sup> occupancy on the (P/Ge)S<sub>4</sub><sup>3-</sup> tetrahedra, the volumes of the tetrahedra increase due to the larger ionic radius of Ge<sup>4+</sup> vs P<sup>5+</sup>, i.e., 0.39 pm vs 0.19 pm,<sup>43</sup> in the tetrahedral coordination (Figure 3c). Another structural characteristic within the argyrodite structure is the possible site disorder between the free S<sup>2-</sup> anion located on Wyckoff 4d and the halide anion I<sup>-</sup> on Wyckoff 4a. While Cl<sup>-</sup> and Br<sup>-</sup>-containing argyrodites show a high degree of anion site disorder, in which the disorder decreases with increasing anionic size mismatch, no disorder had been found for Li<sub>6</sub>PS<sub>5</sub>I due to the large difference in ionic radii between I<sup>-</sup> and S<sup>2-</sup>.<sup>30</sup> Figure 3d shows the I<sup>-</sup>/S<sup>2-</sup> site disorder, as obtained from the Rietveld refinements against X-ray and neutron diffraction data. At a Ge fraction of  $\sim$ 20 at. % there is a clear onset of I<sup>-</sup>/S<sup>2-</sup> site disorder, reaching  $\sim$ 7% around the solubility limit. Whether the changing disorder occurs due to a larger unit cell after Ge<sup>4+</sup> substitution, which allows for better mixing of the mismatched anions, or due to the increasing Li<sup>+</sup> density in the structure remains unclear. Within the series of solid solutions Li<sub>6</sub>PS<sub>5</sub>X (X = Cl, Br, I), a decreasing site disorder due to the incorporation of I<sup>-</sup> is correlated to an increase in the activation barrier for the migrating Li<sup>+</sup> cations,<sup>30</sup> as measured by impedance spectroscopy, and similar effects on the ionic transport may be expected here.

In addition to the structural changes of the (Ge/P)S<sub>4</sub> tetrahedra and I<sup>-</sup>/S<sup>2-</sup> site disorder, the neutron diffraction data allow the analysis of the changes in the Li<sup>+</sup> substructure (Figure 4). With increasing Ge<sup>4+</sup> occupancy, the Li<sup>+</sup> occupancy of the 24g site increases (Figure 4a), and essentially all additional Li<sup>+</sup> occupies this site, similar to the behavior observed for the incorporation of Si<sup>4+</sup> in Li<sub>6</sub>PS<sub>5</sub>Br.<sup>31</sup> The increasing Li occupancy on the 24g site leads to the larger Coulombic repulsion, which results in the longer doublet distance 48h–24g–48h, whereas a minor decrease of the distance between the Li cages (i.e., the intercage distance) can be found. Furthermore, with increasing Li<sup>+</sup> and Ge<sup>4+</sup> content in the structure the tetrahedral volume of Li(48h)S<sub>3</sub>I polyhedra and the area of the Li(24g)S<sub>3</sub> triangular plane increase. As the Li(48h)S<sub>3</sub>I polyhedra represent the bottleneck for the rate-determining intercage jump, the wider diffusion pathways for Li<sup>+</sup> in the structure may affect the mobility of the moving cation.

**Ionic Transport.** Temperature-dependent impedance spectroscopy and nuclear magnetic resonance measurements were performed to assess changes to the ionic conductivity. Arrhenius plots of all samples of Li<sub>6+x</sub>P<sub>1-x</sub>Ge<sub>x</sub>S<sub>5</sub>I and their corresponding impedance responses with the respective fits are shown in Figure 5. The impedance data were fit with an equivalent circuit consisting of one parallel constant phase element (CPE)/resistor in series with a CPE, representing the blocking

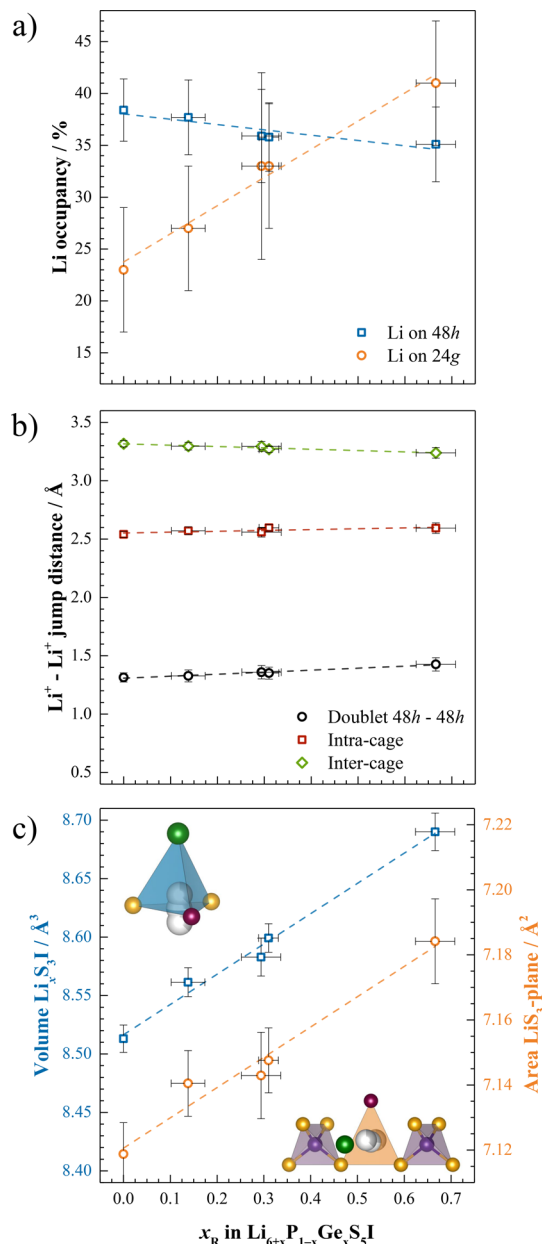


**Figure 4.** Changes to the Li substructure in  $\text{Li}_{6+x}\text{P}_{1-x}\text{Ge}_x\text{S}_3\text{I}$ , as obtained from the neutron diffraction data as a function of the refined Ge content  $x_R$ . With increasing  $\text{Ge}^{4+}$  occupancy, additional  $\text{Li}^+$  is incorporated into the structure to maintain charge neutrality. (a) Percentage of sites occupied by  $\text{Li}^+$  with the additional  $\text{Li}^+$  being placed on the Wyckoff 24g position. (b) The increasing  $\text{Li}^+$  content produces an increase in the distance between the 48h–24g–48 positions (doublet distance), which can be attributed to increased Coulombic repulsion, and a decreasing jump distance between the  $\text{Li}^+$  cages (intercage jump). (c) With increasing unit cell size and size of the adjacent ( $\text{P}/\text{Ge}$ ) $\text{S}_4$  tetrahedra, the  $\text{Li}(48h)\text{S}_3\text{I}$  polyhedra and  $\text{Li}(24g)\text{S}_3$  triangle areas are increasing, corresponding to wider diffusion pathways for  $\text{Li}^+$ .

electrodes. In the samples with a high Ge fraction, the CPE/resistor has shifted to frequencies that are too high to measure with the impedance analyzer, and only the tail of the blocking electrodes was used for the fit. The resolvable impedance spectra exhibit  $\alpha$ -values of  $\sim 0.9$ , representing the ideality of the CPE,<sup>44</sup> and geometric capacitances around 16 to 47  $\mu\text{F cm}^{-2}$ . The extracted values of the impedance analyses are tabulated in the

**Supporting Information (Tables S1–S16).** Bulk and grain boundary contributions cannot be deconvoluted; however, the obtained ideality of the semicircle and capacitances correspond well with bulk transport,<sup>45</sup> as typically observed for these  $\text{Li}^+$  conducting argyrodites.<sup>30,31</sup>

**Figure 6** shows the ionic conductivities of  $\text{Li}_{6+x}\text{P}_{1-x}\text{Ge}_x\text{S}_3\text{I}$ , as measured by impedance spectroscopy, as well as the extracted activation barrier for  $\text{Li}^+$  migration. With increasing fraction of  $\text{Ge}^{4+}$  and  $\text{Li}^+$ , the conductivity increases over 3 orders of magnitude and reaches a maximum conductivity of  $\sigma = 5.4 \pm 0.8 \text{ mS cm}^{-1}$  for  $\text{Li}_{6.6}\text{P}_{0.4}\text{Ge}_{0.6}\text{S}_3\text{I}$ . As the observed increase in the conductivity cannot be directly explained by the minor increase in charge carrier density, the activation energy must be having a tremendous influence. With increasing  $x$ , the activation barrier remains constant at first and then significantly drops, showing an inflection around  $x_R = 0.25$  that is responsible for the high ionic conductivity in the Ge-substituted  $\text{Li}_{6+x}\text{P}_{1-x}\text{Ge}_x\text{S}_3\text{I}$ . Sintering of the cold pressed pellets at 823 K for 10 min increases the conductivity further to  $\sigma = 18.4 \pm 2.7 \text{ mS cm}^{-1}$ , likely due to better grain contact. The variance in the conductivity is calculated from multiple measurements conducted with different measurement setups to corroborate these high conductivity values (see Supporting Information Figure S2).

In addition to the impedance data, selected sample compositions were investigated using  $^7\text{Li}$  nuclear magnetic resonance spectroscopy. **Figure 7a** shows changes of the signal line width as a function of temperature for three measured samples with the compositions of  $x = 0.0$ ,  $0.25$ , and  $0.6$  in  $\text{Li}_{6+x}\text{P}_{1-x}\text{Ge}_x\text{S}_3\text{I}$ , chosen for their different activation barriers (*vide infra*). Only  $\text{Li}_6\text{PS}_3\text{I}$  demonstrates significant dependence of the signal width, whereas the fwhh for all other samples appears to be rather small, even at the lowest available temperatures. Line narrowing starts when the mobility of nuclei in frequency units matches the line width in the rigid limit (a plateau at very low temperatures). Thus, one can estimate the activation energy and the speed of the local ionic motion. As a low-temperature plateau is only observed in the  $\text{Li}_6\text{PS}_3\text{I}$  sample, the Hendrickson–Bray approach<sup>46</sup> can be used to obtain motional parameters in this composition. For the undoped  $\text{Li}_6\text{PS}_3\text{I}$  this procedure gives an estimation of the activation energy of 0.49 eV (**Figure 7b**). The frequency of the corresponding motion can be extrapolated to room temperature and is found to be  $1 \times 10^6 \text{ s}^{-1}$ . In contrast, samples with  $x = 0.25$  and  $x = 0.6$  undergo much faster motional processes, which cannot be characterized with the current method. Therefore,  $T_1$  relaxation time studies (for more information see the Nuclear Magnetic Resonance section in the Supporting Information) are employed to expand the sensitivity window of the dynamical NMR to nanoseconds. The samples with  $x = 0$  and  $x = 0.6$  can be accurately fitted with a single symmetric curve around the maximum, indicating equal  $E_a$  values at high and low temperatures. However, the sample with  $x = 0.25$  reveals different slopes for both flanks, which can be attributed to the coexistence of two types of motion. The first one is activated at lower temperatures and has an activation energy of  $E_a^{\text{LT}} = 0.11 \text{ eV}$ , and another one appears at higher temperatures and is characterized by  $E_a^{\text{HT}} = 0.21 \text{ eV}$ . All  $T_1$ -defined dynamical parameters and analysis procedures are listed in the Supporting Information (Table S18).

Assuming that  $\text{Li}^+$  transport consists of hops between well-defined crystallographic sites, there are three different jump processes possible in  $\text{Li}_6\text{PS}_3\text{X}$  argyrodites, i.e., the doublet 48h jumps, the intracage, and the intercage movements. Moreover,

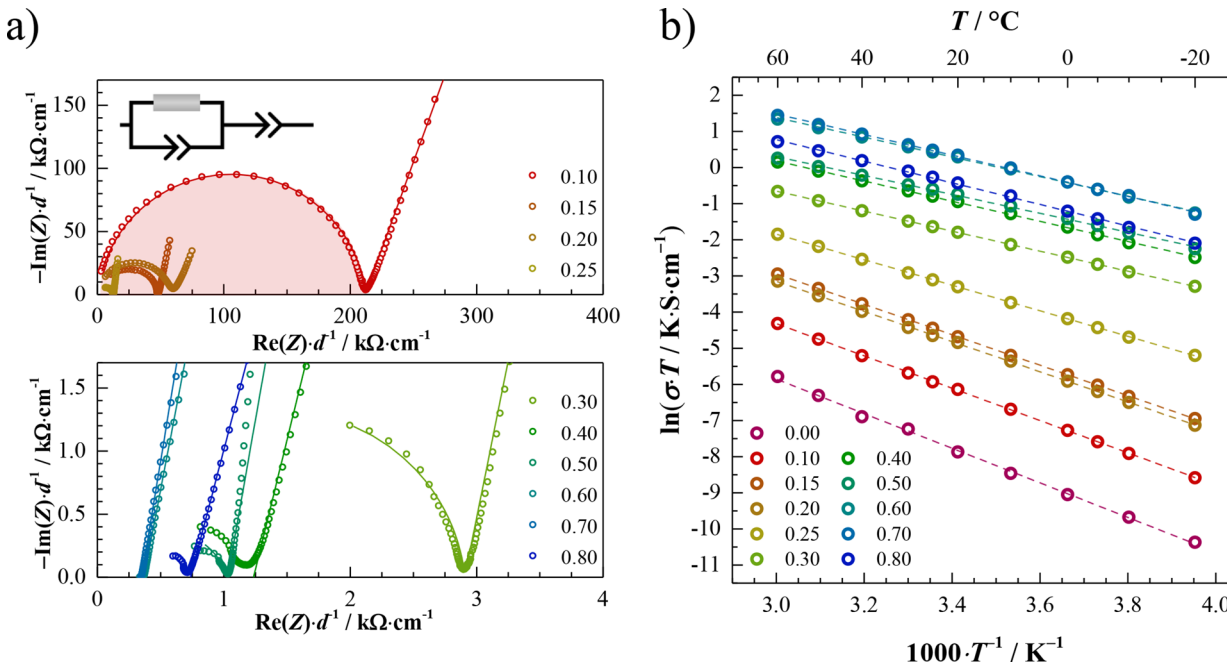


**Figure 5.** (a) Nyquist plots for all degrees of substitution along the series of solid solutions at 298 K, as well as the employed equivalent circuit. The resistance has been normalized to the respective pellet thickness  $d$  for visual comparison. (b) Arrhenius plots of the conductivity values for  $\text{Li}_{6+x}\text{P}_{1-x}\text{Ge}_x\text{S}_5\text{I}$  ( $0 \leq x \leq 0.8$ ).

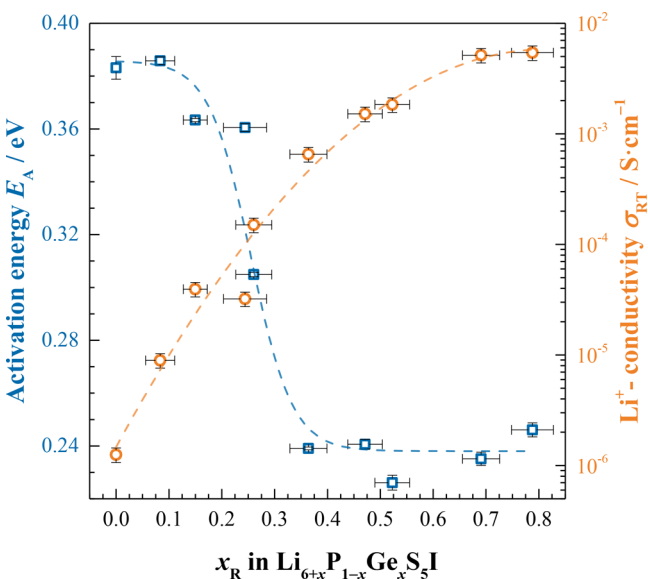


**Figure 6.** Activation barrier and ionic conductivity of  $\text{Li}_{6+x}\text{P}_{1-x}\text{Ge}_x\text{S}_5\text{I}$  as a function of the refined Ge content, as obtained from impedance spectroscopy. With increasing  $\text{Ge}^{4+}$  and  $\text{Li}^+$  concentration, the ionic conductivity increases over 3 orders of magnitude, reaching a conductivity of  $\sigma = 5.4 \text{ mS cm}^{-1}$ . An inflection point starting at  $\sim 20\%$  Ge can be seen that leads to a strong decrease of the activation barrier.

while all jumps are necessary for the long-range transport of  $\text{Li}^+$  ions,<sup>33</sup> intercage jumps have been proposed to be the rate-determining step. Combining this knowledge with the results of our dynamical NMR studies, one can describe the motional picture in the Ge-doped samples. The undoped  $\text{Li}_6\text{PS}_5\text{I}$  undergoes two different motional changes in the  $\mu\text{s}-\text{ns}$  time scale. We suppose that the faster (visible in  $T_1$  relaxation) corresponds to the  $48h-24g-48h$  (doublet jumps) or  $48h-48h$

(intracage jumps) and does not lead to long-range transfer of the  $\text{Li}^+$  ions. In contrast, the slower mobility, which becomes apparent in motional narrowing experiments, is characterized by a much higher activation energy and will be the limiting step in the observable bulk transport, i.e., the intercage jump. The Einstein–Smoluchowski and Nernst–Einstein equations can be used to estimate the conductivity of the sample.<sup>47,48</sup> First, the diffusion coefficient ( $D$ ) is defined from the frequency of motion ( $K_{\text{exchange}}$ ) and the distance between Li sites  $d_{\text{Li-Li}}$  as obtained from the Rietveld refinement of neutron diffraction data:

$$D = \frac{d_{\text{Li-Li}}^2}{6} K_{\text{exchange}} \quad (1)$$

Assuming ion jumps are uncorrelated,<sup>49,50</sup> the conductivity is calculated via

$$\sigma = \frac{DNq}{k_B T} \quad (2)$$

where  $N$  is the charge carrier density approximated by the number of  $\text{Li}^+$  ions per unit cell,  $q$  is the charge of the charge carriers, and  $T$  is the temperature. Based on these equations, a conductivity of  $2.6 \times 10^{-5} \text{ S cm}^{-1}$  at room temperature can be estimated for  $\text{Li}_6\text{PS}_5\text{I}$ , close to the ionic conductivity obtained via impedance spectroscopy.

Although NMR on the sample  $\text{Li}_{6.25}\text{P}_{0.75}\text{Ge}_{0.25}\text{S}_5\text{I}$  also reveals two separate processes, which are likewise described by different activation energies, both modes are visible only in  $T_1$ -relaxation measurements, suggesting much faster rates than those existing in the undoped sample. We propose that the mode with an activation energy of 0.11 eV corresponds to small fluctuations between  $48h$  and  $24g$  sites or the intracage jump process, and the second process can be ascribed to intercage jumps. The sample with a Ge content of 0.6 undergoes a single motional process in the current time scale window with rather low activation energy, in good agreement with the data from impedance spectroscopy.

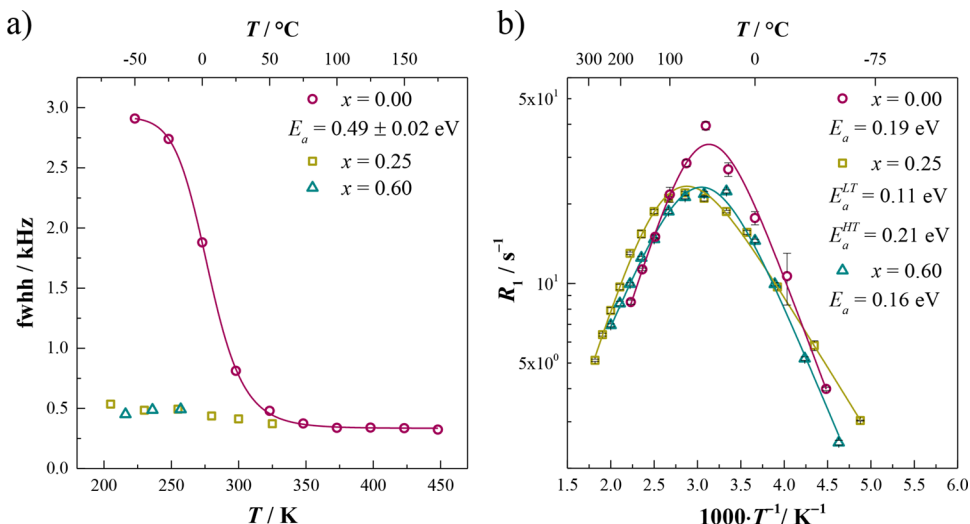


**Figure 7.** (a) Temperature-induced line narrowing of highlighted samples from NMR quadrupolar-echo experiments. (b) Relaxation rates  $R_1$  as a function of inverse temperature and the activation barriers as the result of the fitting procedure (solid lines).

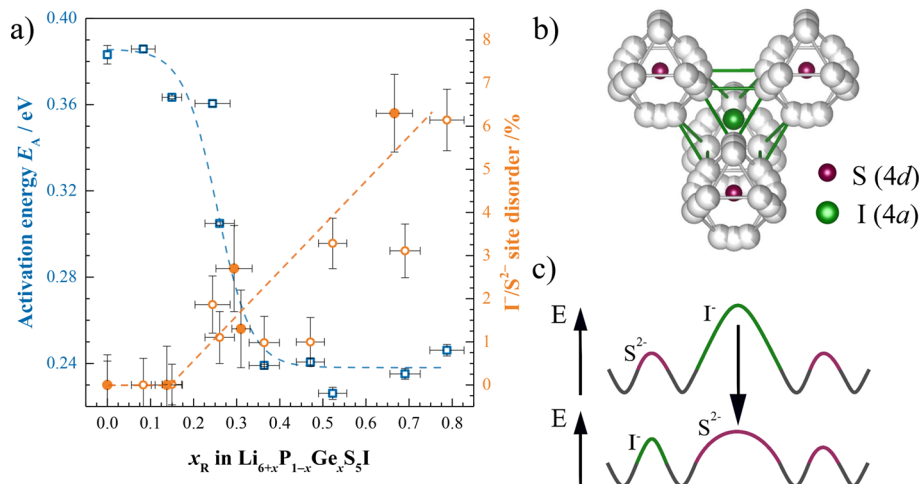


**Figure 8.** (a) Activation barriers and refined  $S^{2-}/I^-$  disorder of  $\text{Li}_{6+x}\text{P}_{1-x}\text{Ge}_x\text{S}_5\text{I}$  as a function of  $x_R$ . At the onset of the occurring  $S^{2-}/I^-$  disorder the activation barriers drop sharply, leading to a high ionic conductivity. (b) Local environment of four  $\text{Li}^+$  clusters around the  $S^{2-}/I^-$  site Wyckoff 4a and (c) schematic of how the potential energy landscape of the migrating ion changes once site disorder occurs. Around the  $S^{2-}/I^-$  position, six total jumps (three spatially distinct, i.e., starting from a different  $\text{Li}^+$ ) can occur to the neighboring three  $\text{Li}^+$  clusters.

We suppose that this corresponds to intercage jumps, whereas all smaller scale movements stay outside of the sensitivity window of the method. Using eqs 1 and 2, a conductivity of 3.9 mS cm<sup>-1</sup> can be estimated for  $x = 0.25$  and 7.5 mS cm<sup>-1</sup> for  $x = 0.6$  in  $\text{Li}_{6+x}\text{P}_{1-x}\text{Ge}_x\text{S}_5\text{I}$ . Overall, the estimated Li-ion conductivities obtained here are in good agreement with the conductivities measured via impedance spectroscopy, suggesting the reduction in the activation energy of the rate-limiting intercage jumps is key to the high conductivity. The slight discrepancy in the conductivity obtained by impedance spectroscopy can likely be attributed to the changing correlation factors with changing Li<sup>+</sup> carrier density.<sup>49,51</sup>

**Structure-Transport Correlation.** The collected data on the aliovalent substitution of  $\text{Li}_{6+x}\text{P}_{1-x}\text{Ge}_x\text{S}_5\text{I}$  show that simple substitutions can have a tremendous influence on the ionic transport in the argyrodite structure and that a high conductivity in the solid electrolytes can be obtained. Impedance spectroscopy and nuclear magnetic resonance data show a decrease in the activation barrier for ionic motion with the inflection point around  $x_R = 0.25$ . In addition, the structural data obtained by

Rietveld refinements against neutron and X-ray diffraction data show an increasing width of the diffusion pathway and an increase in the  $I^-/S^{2-}$  site disorder. In Figure 8a, the changing activation barriers are shown together with the changing of  $I^-/S^{2-}$  site disorder on Wyckoff 4a. There is a clear correlation between the onset of the site disorder and the drop in the activation barrier. As recently theoretically suggested<sup>33</sup> and experimentally corroborated,<sup>30</sup> disorder between the free sulfur site (Wyckoff 4d) and the halide site (Wyckoff 4a) leads to lower activation barriers. In  $\text{Li}_6\text{PS}_5\text{Br}_{1-x}\text{I}_x$ , Kraft et al.<sup>30</sup> were able to show that a subsequent replacement of Br<sup>-</sup> with I<sup>-</sup> leads to fewer halide anions on the free sulfur site and vice versa, resulting in an increasing activation barrier for ionic motion. In this work, the occurrence of disorder leads to a sharp decrease of the activation barrier.

Despite the clear correlation between the disorder and the decreasing activation barrier, it remains puzzling that such a small degree of disorder can affect the transport so significantly. Both Wyckoff positions for I<sup>-</sup> and S<sup>2-</sup> form interpenetrating face-centered cubic lattices, in which the bond-percolation

threshold in one face-centered cube is expected at 12% disorder.<sup>52</sup> However, Figure 8b shows that the Li<sup>+</sup> ions surround the S<sup>2-</sup> site, forming four clusters that are directly linked to the I<sup>-</sup> site. Each cluster faces the I<sup>-</sup> site with three possible 48*h* positions of Li<sup>+</sup>, and from each cluster six jumps are possible to clusters adjacent to the same I<sup>-</sup> position. Each S<sup>2-</sup> on the I<sup>-</sup> site (Wyckoff 4*a*) then opens up three low-energy intercage pathways (see Figure 8c), and percolation would then be expected at 4% for a random distribution. In other words, the high multiplicity of the Li<sup>+</sup> site seemingly makes percolation possible, even at low degrees of disorder. This change in the local environment of Li<sup>+</sup> and the changing potential energy landscape are schematically shown in Figure 8c.

The here-observed correlation between the site disorder and the activation barrier shows that structural changes can have a tremendous influence on the ionic transport in argyrodites. In this example of Li<sub>x</sub>PS<sub>5</sub>X, tailoring the disorder in such materials clearly helps to optimize solid electrolytes toward higher ionic conductivities.

**Solid-State Battery.** Successful implementation of solid-state batteries requires maximizing the energy densities, making thick electrode configurations necessary.<sup>19</sup> While the conductivity of the sintered Li<sub>6.6</sub>P<sub>0.4</sub>Ge<sub>0.6</sub>S<sub>5</sub>I is the highest Li<sup>+</sup> conductivity reported in the argyrodites so far, solid-state batteries employing thiophosphates commonly use cold-pressed electrolytes, so this high conductivity value for the sintered sample will not be utilized in a practical all-solid-state battery setup. Therefore, using the cold-pressed fast conducting Li<sub>6.6</sub>P<sub>0.4</sub>Ge<sub>0.6</sub>S<sub>5</sub>I, solid-state cells were constructed with thick cathode and anode composites. The cathode has an approximate thickness of 160 μm and the anode, having a higher SE fraction, is estimated to be 340 μm thick (Figure 9d). The separator thickness is approximately 450 μm. At a charging rate of 0.25 C and a temperature of 60 °C, the thick electrode cell offers an initial charging capacity of 120.8 mAh g<sup>-1</sup>. The initial discharge capacity is 88.8 mAh g<sup>-1</sup>, which stabilizes to 99.3 mAh g<sup>-1</sup> in the subsequent cycles, indicating a beneficial interphase formation (Figure 9a and b).<sup>8–10</sup> Without the addition of carbon additives or protective interfacial modifications,<sup>14</sup> the cell shows stable cycling with little to no capacity fade over 50 cycles, maintaining a very high Coulombic efficiency. The stability of the capacity is even obtained when increasing the C-rate to 0.5 C and even further to 1 C, upon cycling for 50 additional cycles at each rate. Despite this thick electrode configuration, the total resistance of the cell is below 13 Ω cm<sup>-2</sup> at 60 °C (see Supporting Information Figure S3). The herein presented cell demonstrates the feasibility of high and stable performances when employing a superionic thiophosphate solid electrolyte with nondetrimental interphase formation.

#### 4. CONCLUSION

In this work, aliovalent substitution in Li<sub>6+x</sub>P<sub>1-x</sub>Ge<sub>x</sub>S<sub>5</sub>I was performed, and the changes to the structure and transport were investigated. Using a combination of X-ray and neutron diffraction, nuclear magnetic resonance, and impedance spectroscopy, the lattice variations, Ge solubility, and, more specifically, the Li<sup>+</sup> occupancies and I<sup>-</sup>/S<sup>2-</sup> site disorder were monitored. With increasing Ge content, a significant change in the activation barrier was observed, which coincides with an increase of the I<sup>-</sup>/S<sup>2-</sup> site disorder. The structural changes and increasing lattice volume lead to an opening of the bottle necks, and nuclear magnetic resonance indicates more facile intercage jumps. The interpenetration of face-centered-cubic lattices in

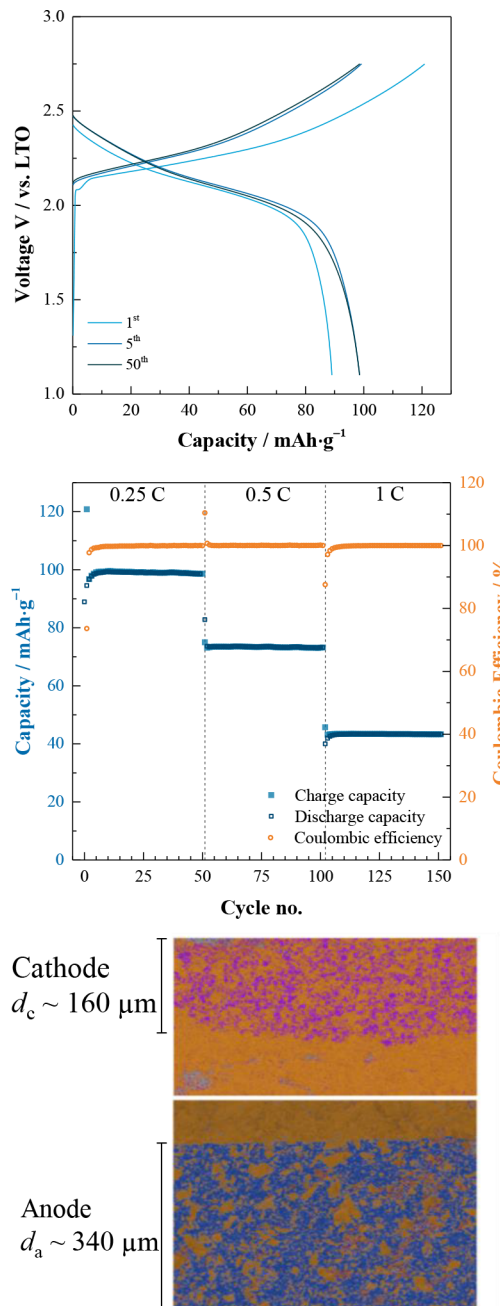


**Figure 9.** (a) Representative charge and discharge curves of the thick electrode cell for the first, fifth, and 50th cycles. (b) Charge and discharge capacities (blue rectangles) over 150 cycles and corresponding Coulombic efficiency (orange circles). After a formation period within the first 5 cycles, the cell offers a stable capacity and cycling efficiency. (c) EDX mapping of the cathode (top) and anode (bottom) cross sections for the all-solid-state battery. The solid electrolyte is represented by the sulfur signal (orange). The NCM-622 cathode is represented by the Ni signal (purple), and the LTO anode by the O signal (blue), respectively.

the argyrodite structure means that only a low degree of disorder is needed to reach the percolation threshold. The drop in the activation barrier due to these structural changes leads to a high ionic conductivity of  $5.4 \pm 0.8 \text{ mS cm}^{-1}$  in Li<sub>6.6</sub>P<sub>0.4</sub>Ge<sub>0.6</sub>S<sub>5</sub>I, and sintering of the pellets can further increase the ionic conductivity to  $18.4 \pm 2.7 \text{ mS cm}^{-1}$ . With these high-performance solid electrolytes, solid-state batteries with thick electrode config-

urations were successfully cycled, showing no apparent capacity fade over 150 cycles.

This work shows that structural changes and site disorder can be used to induce severe changes in the potential energy landscape. These structural changes strongly affect the activation barrier for the mobile ions, which helps to further optimize electrolytes towards obtaining high ionic conductivities and allows their practical use in thick-electrode cells for solid-state battery applications.

## ■ ASSOCIATED CONTENT

### § Supporting Information

The Supporting Information is available free of charge on the ACS Publications website at DOI: [10.1021/jacs.8b10282](https://doi.org/10.1021/jacs.8b10282).

All refined diffraction data; stacked plots of the diffraction data as well as the tabulated results from NMR and impedance spectroscopy; information on the fitting of the NMR  $T_1$  relaxation rate; measurements of the sintered materials in multiple measurement setups and geometries; impedance data of the solid-state battery cells ([PDF](#))

## ■ AUTHOR INFORMATION

### Corresponding Author

\*[wolfgang.g.zeier@pc.jlug.de](mailto:wolfgang.g.zeier@pc.jlug.de)

### ORCID

Saneyuki Ohno: 0000-0001-8192-996X

Sylvio Indris: 0000-0002-5100-113X

Wolfgang G. Zeier: 0000-0001-7749-5089

### Notes

The authors declare no competing financial interest.

## ■ ACKNOWLEDGMENTS

The research was supported by the Deutsche Forschungsgemeinschaft (DFG) under grant number ZE 1010/4-1. S.C. gratefully acknowledges the Alexander von Humboldt Foundation for financial support through a Postdoctoral Fellowship. We thank BASF SE for the supply of the electrode materials to perform solid-state battery testing.

## ■ REFERENCES

- (1) Janek, J.; Zeier, W. G. A Solid Future for Battery Development. *Nat. Energy* **2016**, *1*, 16141.
- (2) Culver, S. P.; Krauskopf, T.; Koerver, R.; Zeier, W. G. Designing Ionic Conductors: The Interplay between Structural Phenomena and Interfaces in Thiophosphate-Based Solid-State Batteries. *Chem. Mater.* **2018**, *30*, 4179–4192.
- (3) Jung, Y. S.; Oh, D. Y.; Nam, Y. J.; Park, K. H. Issues and Challenges for Bulk-Type All-Solid-State Rechargeable Lithium Batteries Using Sulfide Solid Electrolytes. *Isr. J. Chem.* **2015**, *55*, 472–485.
- (4) Zhang, Z.; Shao, Y.; Lotsch, B. V.; Hu, Y.-S.; Li, H.; Janek, J.; Nan, C.; Nazar, L.; Maier, J.; Armand, M.; Chen, L. New Horizons for Inorganic Solid State Ion Conductors. *Energy Environ. Sci.* **2018**, *11*, 1945–1976.
- (5) Park, K. H.; Bai, Q.; Kim, D. H.; Oh, D. Y.; Zhu, Y.; Mo, Y. Design Strategies, Practical Considerations, and New Solution Processes of Sulfide Solid Electrolytes for All-Solid-State Batteries. *Adv. Energy Mater.* **2018**, *8*, 1800035.
- (6) Kato, Y.; Hori, S.; Saito, T.; Suzuki, K.; Hirayama, M.; Mitsui, A.; Yonemura, M.; Iba, H.; Kanno, R. High-Power All-Solid-State Batteries Using Sulfide Superionic Conductors. *Nat. Energy* **2016**, *1*, 16030.
- (7) Goodenough, J. B.; Park, K.-S. The Li-Ion Rechargeable Battery: A Perspective. *J. Am. Chem. Soc.* **2013**, *135*, 1167–1176.
- (8) Zhang, W.; Weber, D. A.; Weigand, H.; Arlt, T.; Manke, I.; Schröder, D.; Koerver, R.; Leichtweiss, T.; Hartmann, P.; Zeier, W. G.; Janek, J. Interfacial Processes and Influence of Composite Cathode Microstructure Controlling the Performance of All-Solid-State Lithium Batteries. *ACS Appl. Mater. Interfaces* **2017**, *9*, 17835–17845.
- (9) Koerver, R.; Walther, F.; Akgün, I.; Sann, J.; Dietrich, C.; Zeier, W. G.; Janek, J. Redox-Active Cathode Interphases in Solid-State Batteries. *J. Mater. Chem. A* **2017**, *5*, 22750–22760.
- (10) Koerver, R.; Akgün, I.; Leichtweiss, T.; Dietrich, C.; Zhang, W.; Binder, J. O.; Hartmann, P.; Zeier, W. G.; Janek, J. Capacity Fade in Solid-State Batteries: Interphase Formation and Chemomechanical Processes in Nickel-Rich Layered Oxide Cathodes and Lithium Thiophosphate Solid Electrolytes. *Chem. Mater.* **2017**, *29*, 5574–5582.
- (11) Okada, K.; Machida, N.; Naito, M.; Shigematsu, T.; Ito, S.; Fujiki, S.; Nakano, M.; Aihara, Y. Preparation and Electrochemical Properties of  $\text{LiAlO}_2$ -Coated  $\text{Li}(\text{Ni}_{1/3}\text{Mn}_{1/3}\text{Co}_{1/3})\text{O}_2$  for All-Solid-State Batteries. *Solid State Ionics* **2014**, *255*, 120–127.
- (12) Machida, N.; Kashiwagi, J.; Naito, M.; Shigematsu, T. Electrochemical Properties of All-Solid-State Batteries with  $\text{ZrO}_2$ -Coated  $\text{LiNi}_{1/3}\text{Mn}_{1/3}\text{Co}_{1/3}\text{O}_2$  as Cathode Materials. *Solid State Ionics* **2012**, *225*, 354–358.
- (13) Yoon, K.; Kim, J.; Seong, W. M.; Lee, M. H.; Kang, K. Investigation on the Interface between  $\text{Li}_{10}\text{GeP}_2\text{S}_{12}$  Electrolyte and Carbon Conductive Agents in All-Solid-State Lithium Battery. *Sci. Rep.* **2018**, *8*, 8066.
- (14) Zhang, W.; Leichtweiss, T.; Culver, S. P.; Koerver, R.; Das, D.; Weber, D. A.; Zeier, W. G.; Janek, J. The Detrimental Effects of Carbon Additives in  $\text{Li}_{10}\text{GeP}_2\text{S}_{12}$ -Based Solid-State Batteries. *ACS Appl. Mater. Interfaces* **2017**, *9*, 35888–35896.
- (15) Strauss, F.; Bartsch, T.; De Biasi, L.; Kim, A. Y.; Janek, J.; Hartmann, P.; Brezesinski, T. Impact of Cathode Material Particle Size on the Capacity of Bulk-Type All-Solid-State Batteries. *ACS Energy Lett.* **2018**, *3*, 992–996.
- (16) Sakuda, A.; Takeuchi, T.; Kobayashi, H. Electrode Morphology in All-Solid-State Lithium Secondary Batteries Consisting of  $\text{LiNi}_{1/3}\text{Co}_{1/3}\text{Mn}_{1/3}\text{O}_2$  and  $\text{Li}_2\text{S}-\text{P}_2\text{S}_5$  Solid Electrolytes. *Solid State Ionics* **2016**, *285*, 112–117.
- (17) Zhang, W.; Schröder, D.; Arlt, T.; Manke, I.; Koerver, R.; Pinedo, R.; Weber, D. A.; Sann, J.; Zeier, W. G.; Janek, J. (Electro)Chemical Expansion during Cycling: Monitoring the Pressure Changes in Operating Solid-State Lithium Batteries. *J. Mater. Chem. A* **2017**, *5*, 9929–9936.
- (18) Koerver, R.; Zhang, W.; de Biasi, L.; Schweidler, S.; Kondrakov, A. O.; Kolling, S.; Brezesinski, T.; Hartmann, P.; Zeier, W. G.; Janek, J. Chemo-Mechanical Expansion of Lithium Electrode Materials – on the Route to Mechanically Optimized All-Solid-State Batteries. *Energy Environ. Sci.* **2018**, *11*, 2142–2158.
- (19) Kato, Y.; Shiotani, S.; Morita, K.; Suzuki, K.; Hirayama, M.; Kanno, R. All-Solid-State Batteries with Thick Electrode Configurations. *J. Phys. Chem. Lett.* **2018**, *9*, 607–613.
- (20) Dietrich, C.; Weber, D. A.; Sedlmaier, S. J.; Indris, S.; Culver, S. P.; Walter, D.; Zeier, W. G. Lithium Ion Conductivity in  $\text{Li}_2\text{S}$  –  $\text{P}_2\text{S}_5$  Glasses. *J. Mater. Chem. A* **2017**, *5*, 18111–18119.
- (21) Tatsumisago, M.; Hayashi, A. Sulfide Glass-Ceramic Electrolytes for All-Solid-State Lithium and Sodium Batteries. *Int. J. Appl. Glas. Sci.* **2014**, *10*, 226–235.
- (22) Kamaya, N.; Homma, K.; Yamakawa, Y.; Hirayama, M.; Kanno, R.; Yonemura, M.; Kamiyama, T.; Kato, Y.; Hama, S.; Kawamoto, K.; Mitsui, A. A Lithium Superionic Conductor. *Nat. Mater.* **2011**, *10*, 682–686.
- (23) Bron, P.; Johansson, S.; Zick, K.; Schmedt auf der Günne, J.; Dehnen, S.; Roling, B.  $\text{Li}_{10}\text{SnP}_2\text{S}_{12}$ : An Affordable Lithium Superionic Conductor. *J. Am. Chem. Soc.* **2013**, *135*, 15694–15697.
- (24) Kato, Y.; Saito, R.; Sakano, M.; Mitsui, A.; Hirayama, M.; Kanno, R. Synthesis, Structure and Lithium Ionic Conductivity of Solid Solutions of  $\text{Li}_{10}(\text{Ge}_{1-x}\text{M}_x)\text{P}_2\text{S}_{12}$  ( $\text{M} = \text{Si}, \text{Sn}$ ). *J. Power Sources* **2014**, *271*, 60–64.

- (25) Krauskopf, T.; Culver, S. P.; Zeier, W. G. Bottleneck of Diffusion and Inductive Effects in  $\text{Li}_{10}\text{Ge}_{1-x}\text{Sn}_x\text{P}_2\text{S}_{12}$ . *Chem. Mater.* **2018**, *30*, 1791–1798.
- (26) Weber, D. A.; Senyshyn, A.; Weldert, K. S.; Wenzel, S.; Zhang, W.; Kaiser, R.; Berendts, S.; Janek, J.; Zeier, W. G. Structural Insights and 3D Diffusion Pathways within the Lithium Superionic Conductor  $\text{Li}_{10}\text{GeP}_2\text{S}_{12}$ . *Chem. Mater.* **2016**, *28*, 5905–5915.
- (27) Kuhn, A.; Koehler, J.; Lotsch, B. V. Single-Crystal X - Ray Structure Analysis of the Superionic Conductor  $\text{Li}_{10}\text{GeP}_2\text{S}_{12}$ . *Phys. Chem. Chem. Phys.* **2013**, *15*, 11620–11622.
- (28) Kuhn, A.; Gerbig, O.; Zhu, C.; Falkenberg, F.; Maier, J.; Lotsch, B. V. A New Ultrafast Superionic Li-Conductor: Ion Dynamics in  $\text{Li}_{11}\text{Si}_2\text{PS}_{12}$  and Comparison with Other Tetragonal LGPS-Type Electrolytes. *Phys. Chem. Chem. Phys.* **2014**, *16*, 14669–14674.
- (29) Rangasamy, E.; Liu, Z.; Gobet, M.; Pilar, K.; Sahu, G.; Zhou, W.; Wu, H.; Greenbaum, S.; Liang, C. An Iodide-Based  $\text{Li}_3\text{P}_2\text{S}_8\text{I}$  Superionic Conductor. *J. Am. Chem. Soc.* **2015**, *137*, 1384–1387.
- (30) Kraft, M. A.; Culver, S. P.; Calderon, M.; Böcher, F.; Krauskopf, T.; Senyshyn, A.; Dietrich, C.; Zevalkink, A.; Janek, J.; Zeier, W. G. Influence of Lattice Polarizability on the Ionic Conductivity in the Lithium Superionic Argyrodites  $\text{Li}_6\text{PS}_5\text{X}$  ( $\text{X} = \text{Cl}, \text{Br}, \text{I}$ ). *J. Am. Chem. Soc.* **2017**, *139*, 10909–10918.
- (31) Minafra, N.; Culver, S. P.; Krauskopf, T.; Senyshyn, A.; Zeier, W. G. Effect of Si Substitution on the Structural and Transport Properties of Superionic Li-Arnyrodites. *J. Mater. Chem. A* **2018**, *6*, 645–651.
- (32) Deiseroth, H. J.; Kong, S. T.; Eckert, H.; Vannahme, J.; Reiner, C.; Zaif, T.; Schlosser, M.  $\text{Li}_6\text{PS}_5\text{X}$ : A Class of Crystalline Li-Rich Solids with an Unusually High  $\text{Li}^+$  Mobility. *Angew. Chem., Int. Ed.* **2008**, *47*, 755–758.
- (33) de Clerk, N. J. J.; Roslón, I.; Wagemaker, M. Diffusion Mechanism of Li Arnyrodite Solid Electrolytes for Li-Ion Batteries and Prediction of Optimized Halogen Doping: The Effect of Li Vacancies, Halogens, and Halogen Disorder. *Chem. Mater.* **2016**, *28*, 7955–7963.
- (34) Chen, H. M.; Maohua, C.; Adams, S. Stability and Ionic Mobility in Arnyrodite-Related Lithium-Ion Solid Electrolytes. *Phys. Chem. Chem. Phys.* **2015**, *17*, 16494–16506.
- (35) Catlow, C. R. Static Lattice Simulation of Structure and Transport in Superionic Conductors. *Solid State Ionics* **1983**, *8*, 89–107.
- (36) Rayavarapu, P. R.; Sharma, N.; Peterson, V. K.; Adams, S. Variation in Structure and  $\text{Li}^+$ -Ion Migration in Arnyrodite-Type  $\text{Li}_6\text{PS}_5\text{X}$  ( $\text{X} = \text{Cl}, \text{Br}, \text{I}$ ) Solid Electrolytes. *J. Solid State Electrochem.* **2012**, *16*, 1807–1813.
- (37) Hoelzel, M.; Senyshyn, A.; Dolotko, O. SPODI: High Resolution Powder Diffractometer. *JLSRF* **2015**, *1*, 5.
- (38) Hoelzel, M.; Senyshyn, A.; Juenke, N.; Boysen, H.; Schmahl, W.; Fuess, H. High-Resolution Neutron Powder Diffractometer SPODI at Research Reactor FRM II. *Nucl. Instrum. Methods Phys. Res., Sect. A* **2012**, *667*, 32–37.
- (39) Coelho, A. A. *TOPAS-Academic*; Brisbane, Australia, 2007.
- (40) Thompson, P.; Cox, D. E.; Hastings, J. B. Rietveld Refinement of Debye-Scherrer Synchrotron X-Ray Data from  $\text{Al}_2\text{O}_3$ . *J. Appl. Crystallogr.* **1987**, *20* (2), 79–83.
- (41) Young, R. A. *The Rietveld Method*; Oxford University Press: New York, 1993.
- (42) Busche, M. R.; Weber, D. A.; Schneider, Y.; Dietrich, C.; Wenzel, S.; Leichtweiss, T.; Schröder, D.; Zhang, W.; Weigand, H.; Walter, D.; Sedlmaier, S. J.; Houtarde, D.; Nazar, L. F.; Janek, J. In Situ Monitoring of Fast Li-Ion Conductor  $\text{Li}_7\text{P}_3\text{S}_{11}$  Crystallization Inside Hot-Press Setup. *Chem. Mater.* **2016**, *28*, 6152–6165.
- (43) Shannon, R. D. Revised Effective Ionic Radii and Systematic Studies of Interatomic Distances in Halides and Chalcogenides Central Research and Development Department, Experimental Station, E. I. Du Pont de Nemours The Effective Ionic Radii of Shannon & Prewitt [*Acta. Acta Crystallogr., Sect. A: Cryst. Phys., Diffr., Theor. Gen. Crystallogr.*] **1976**, *32*, 751–767.
- (44) Brug, G. J.; van den Eeden, A. L. G.; Sluyters-Rehbach, M.; Sluyters, J. H. The Analysis of Electrode Impedances Complicated by the Presence of a Constant Phase Element. *J. Electroanal. Chem. Interfacial Electrochem.* **1984**, *176*, 275–295.
- (45) Irvine, J. T. S.; Sinclair, D. C.; West, A. R. Electroceramics: Characterization by Impedance Spectroscopy. *Adv. Mater.* **1990**, *2*, 132–138.
- (46) Hendrickson, J. R.; Bray, P. J. A Phenomenological Equation for NMR Motional Narrowing in Solids. *J. Magn. Reson.* **1973**, *9*, 341–357.
- (47) Heitjans, P.; Indris, S. Diffusion and Ionic Conduction in Nanocrystalline Ceramics. *J. Phys.: Condens. Matter* **2003**, *1257*, R1257–R1289.
- (48) Uitz, M.; Epp, V.; Bottke, P.; Wilkening, M. Ion Dynamics in Solid Electrolytes for Lithium Batteries: Probing Jump Rates and Activation Energies through Time-Domain Li NMR. *J. Electroceram.* **2017**, *38*, 142–156.
- (49) Morgan, B. J.; Morgan, B. J. Lattice-Geometry Effects in Garnet Solid Electrolytes: A Lattice-Gas Monte Carlo Simulation Study. *R. Soc. Open Sci.* **2017**, *4*, 170824.
- (50) Murch, G. The Haven Ratio in Fast Ionic Conductors. *Solid State Ionics* **1982**, *7*, 177–198.
- (51) He, X.; Zhu, Y.; Mo, Y. Origin of Fast Ion Diffusion in Super-Ionic Conductors. *Nat. Commun.* **2017**, *8*, 15893.
- (52) Ashcroft, N. W.; Mermin, N. D. *Solid State Physics*; Thomson Learning Inc.: USA, 1976.